A time-average ocean: Thermal wind and flow spirals

Carl Wunsch [*]

Harvard University, Cambridge MA, United States of America
MIT, Cambridge MA, United States of America

ARTICLE INFO

ABSTRACT

Using a 26-year average of a dynamically consistent ECCO state-estimate, an effort is made to find a few simple descriptive, but quantitative, patterns of properties of the ocean circulation that are near-globally applicable outside the Arctic regions. The conceptual assumption is made that such an average is physically meaningful. Even with a 26-year average, complex spatial variations in the flow field remain, particularly below about 2000 m where the intricate structure of the underlying topography becomes manifest. Nonetheless, certain constructs do describe the great bulk of the ocean. These constructs consist of thermal wind balance (quasi-geostrophy), spiral-like flow behavior in the near-surface boundary layers with orientation analogous to that of an Ekman layer—abruptly changing sign across the equator. In contrast, evidence for beta-spirals is very thin, consistent with the spatially complex meridional and vertical velocities. As expected, integration so as to remove spatial dependence in one coordinate (e.g. zonal) does produce much simplified structures, albeit in the process suppressing diverse dynamical regimes. Predominantly zonal structures persist in the zonal velocity at depth, and are presumed sensitive to the (parameterized) mean eddy fluxes. An unanswered question, and one perhaps unanswerable at the present time, is whether a much longer averaging interval would significantly further simplify the upper-ocean circulation. The abyssal circulation almost everywhere appears dominated by the topography and slopes and whose structure likely would persist in averages of arbitrary duration.

1. Introduction

As in a previous paper, Wunsch (2023, hereafter W23) an attempt is made here to extract some simple quantitative patterns that are widely applicable when describing the *time-averaged* global ocean. Present knowledge suggests that the ocean has numerous physically distinct regions, and within those regions each grid point can differ quantitatively from any others—rendering difficult any sort of generalization. As an example of the challenge, W23 addressed the question of whether the Munk "abyssal recipes" were a generally applicable description of the global ocean below about 1000 m? (The answer was "no".) That estimates of synoptic flows are highly complex is widely understood, but the extent of simplification by temporal averaging is unclear.

Results in both W23 and here are based upon a 26-year uniform time-averaged state estimate (version 4, release 4) from the Estimating the Circulation and Climate of the Ocean (ECCOv4r4; see Wunsch and Heimbach, 2007; Forget et al., 2015; Fukumori et al., 2019) with 1° of horizontal spatial resolution. That estimate has the property, up to numerical accuracy, of obeying all of the physically important time-varying constraints of a system, including conservation laws for energy, mass, vorticity, etc. and the usual no-slip and known flux boundary conditions and so is physically realizable through time. "Obeying" is

used in the sense that changes in each of the values of conservation laws can be traced to values and inferred changes in forcing and dissipation mechanisms without incurring the errors in these quantities often induced by methods intended to accommodate sequential observations (Wunsch et al., 2023). The estimate also has the important property that it represents a non-linear least-squares fit of a version of the MITgcm to the great majority of global-scale data sets (CTD, Argo, altimetry, scatterometry, meteorological fields, etc. including their uncertainty estimates; see Forget et al., 2015). An alternative statement of the present goal is to ask "What qualitative, but quantifiable, properties of the time-average ocean circulation must be reproduced by any useful near-global description, including those from general circulation models?" Results are necessarily not exhaustive of the possibilities.

Forget et al. (2015) should be consulted for technical details of the underlying model, data, and the estimation methods. The computation can be thought of as a very large inverse problem, one employing a multitude of primarily interior ocean observations to infer both the general circulation everywhere and adjusted surface meteorological forcing via a turbulence closure represented by the general circulation model. Of particular importance here are the use of the Gaspar et al. (1990) near-surface dynamics, the Gent and Mcwilliams (1990) eddy effects

* Correspondence to: Harvard University, Cambridge MA, United States of America.
   E-mail address: carl.wunsch@gmail.com.

scheme, the Redi (1982) mixing tensor, and other parameterizations of instabilities and mixing. The Appendix has a brief discussion of the role of unresolved boundary layers in the presence of large amounts of interior data (Callies and Ferrari, 2018, is an example). As an inverse problem, best-estimate boundary conditions could be treated as part of the estimated control parameters instead of being imposed, but that extension has not yet been attempted.

A few of the salient phenomena in the global 26-year average are sought, and to determine which properties of the dynamical time-mean solution can, unlike the original abyssal recipes in W23, be used as near-universal descriptors of the near-global ocean. Another example of a hypothetical descriptor would be the statement that in most of the world ocean, the time-mean upper layer velocities describe an Ekman-like spiral (which proves true). An earlier time-average was described by Forget (2010), but over a considerably shorter time interval (3 years). Numerous pictorial renderings of a shorter, 20-year v4r4 average, can be seen in http://hdl.handle.net/1721.1/107613, and http://hdl.handle.net/1721.1/109847 and with a discussion in Fukumori et al. (2018). Many fields not displayed here, as well as a sketch representation of the time-variability, can be found in those references.

Finding explanatory physics underlying most of the results requires analyses that must also be found elsewhere. The present goal does however, require a minimal sketch of the global circulation and its properties. No claim is made that what follows is a full or definitive description of the time-average oceanic general circulation: that requires a much longer and elaborate study. Comparisons could be made, for example, with many of the descriptive elements in Talley et al. (2011)—requiring a book. Decisions as to the most useful pictorial representations of a three- dimensional global flow are extremely challenging, and to a considerable degree, arbitrary.

An underlying conceptual question, is what might be called the "hypothesis of simplification": that is whether a multi-decade time-average of the circulation is necessarily significantly simpler than a synoptic one. On the one hand, averages tend to simplify by diminishing structures arising from temporally varying phenomena. On the other hand, long-term averages permit the emergence – from the masking variability – of quasi-steady structures from the zero-frequency intricate topography and lateral boundaries, and from the influence of inhomogeneities of time-mean forcing and turbulent effects. Which, if any, of these effects will dominate over 26-years and longer is not, a priori, obvious. The simplification hypothesis has a direct bearing e.g., on the utility of a Reynolds decomposition in frequency and/or wavenumber.

Discussion and analysis here are confined to the regions southward of about 60°N—omitting the Arctic regions, which are the subject of a purpose-built state estimation system (Nguyen et al., 2021), one including the important effects of sea ice. Some of the figures do display Arctic structures, but they are not discussed here. Note too, that a higher resolution state estimate of the Southern Ocean region (Mazloff et al., 2010) and subsequent published analyses of the physics also exist. Much higher resolution global state estimates are available (Menemenlis et al., 2008), but for considerably shorter intervals than being used here. Those are being incrementally extended in time without data constraints – apart from the initial conditions – as derived from ECCOv4.[1]

---

[1] For recent developments in the higher resolution representation and for biological applications, see Carroll et al. (2022) and for a discussion of the role of resolved eddies on Lagrangian flows, see Wang et al. (2022), among other applications.

1.1. Underlying time scales

Of the powerful and attractive theories of the ocean circulation (e.g., Sverdrup balance, abyssal recipes, Stommel–Arons flows, etc.) almost all were created in the framework of a laminar steady-state ocean, commonly with simplified topography and surface and lateral boundary structures. In recent decades (e.g., the Wunsch and Ferrari, 2018 review, and numerous other papers), it has become clear that the synoptic ocean is turbulent on many scales and filled with fields of three-dimensional structures, often labeled as " eddies" of a great variety of theoretical and observational types – with no known low frequency cut-off – and including such phenomena as surface and internal waves, too.

Known adjustment times of the large-scale ocean vary from days (some barotropic Rossby wave phenomena), decades (high latitude baroclinic adjustments), and out to many thousands of years (water mass property adjustment times). Inferences of multi-decadal variability in many circulation elements are well-known. In that context, 26-years is an extremely short averaging time and the system is surely not in equilibrium (Gebbie, 2021, discusses the issue of thermal equilibrium in the ocean). It is nonetheless of interest to understand the extent to which such an average does reduce the complexity of the system, possibly leading to global generalizations. As a rough guide to the structure of temporal stability, Fig. A2 in the Appendix shows the standard deviation of current speed at the sea-surface computed from annual averages. Many distinct regions appear. The focus on what follows is on the velocity field—including its connection to in situ density through the quasi-geostrophic thermal wind equations. Central results are mostly pictorial and in the interests of a shorter length, some useful figures are consigned to an Appendix.

2. Flow field

Let u, v, w be the zonal, meridional and vertical velocity components, all understood to be 26-year Eulerian time-average values. The descriptions that follow could be done for Lagrangian or residual mean velocities, but the Eulerian picture is the most straightforward and familiar from the classical hydrographic, period. Local cartesian coordinates are x, y, z. Figs. 1, 2 display the horizontal flow elements, u, v at a variety of depths. (The contouring algorithm used in this paper obscures some small scale features.) The 95 m depth shows the conventional features of the near-surface velocity field, including the complex reversing-with-latitude zonal flows near the equator, and the locally intensified patches in the Southern Ocean. The ocean interior meridional flow field at this depth shows the generally equatorward-motion characteristic of Sverdrup balance driven by downward Ekman pumping, in both hemispheres of the Atlantic and Pacific. A very sharp convergence of v is seen at the equator over much of the Pacific and partially so in the Atlantic and Indian Oceans (Brandt et al., 2008, their Fig. 1. describe the intricate flow field expected in the equatorial Atlantic.) In the meridional flow at 635 m, the vertical persistence of the Sverdrup-balance interiors is clear, with equatorward flow in both hemispheres within the major gyres. See Thomas et al. (2014).

By 1100 m several characteristics of the abyssal flows emerge. These include the much greater structure in v as compared to u with the latter still displaying a strong tendency toward a series of quasi-zonal jets. A large literature discusses the formation of zonal jets albeit in the ocean primarily directed at transient features arising from local turbulence (for observations see e.g., Hogg and Owens, 1999; Davis, 2005, and the review by Cornillon et al., 2019). A foundation of dynamical oceanography is the linearized potential vorticity conservation equation,

$$\beta v = f \frac{\partial w}{\partial z}. \tag{1}$$

where f, β are the Coriolis parameter and its meridional derivative. Liang et al. (2017) described the time-average vertical velocity fields,
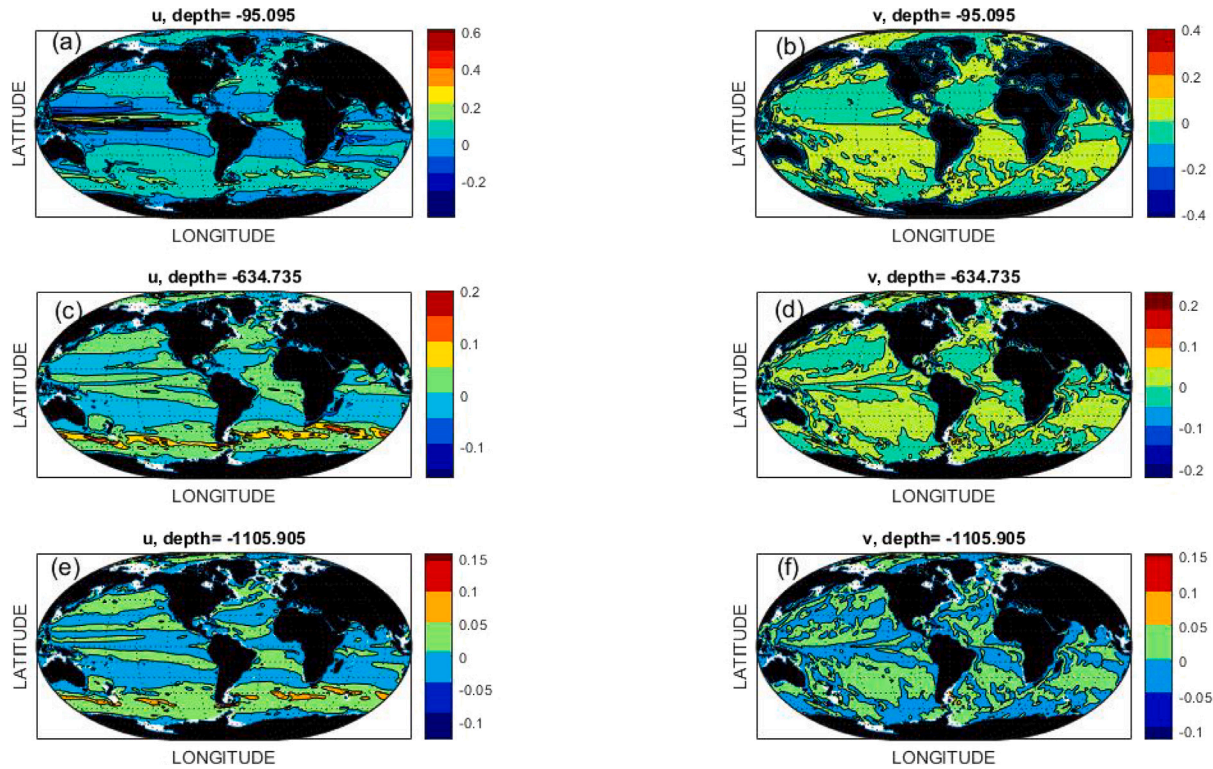
Fig. 1. Time-average zonal velocity (left column) and meridional velocity (right column) at depths (a, b) 95 m, (c, d) 635 m, (e, f) 1100 m. Units are m/s.
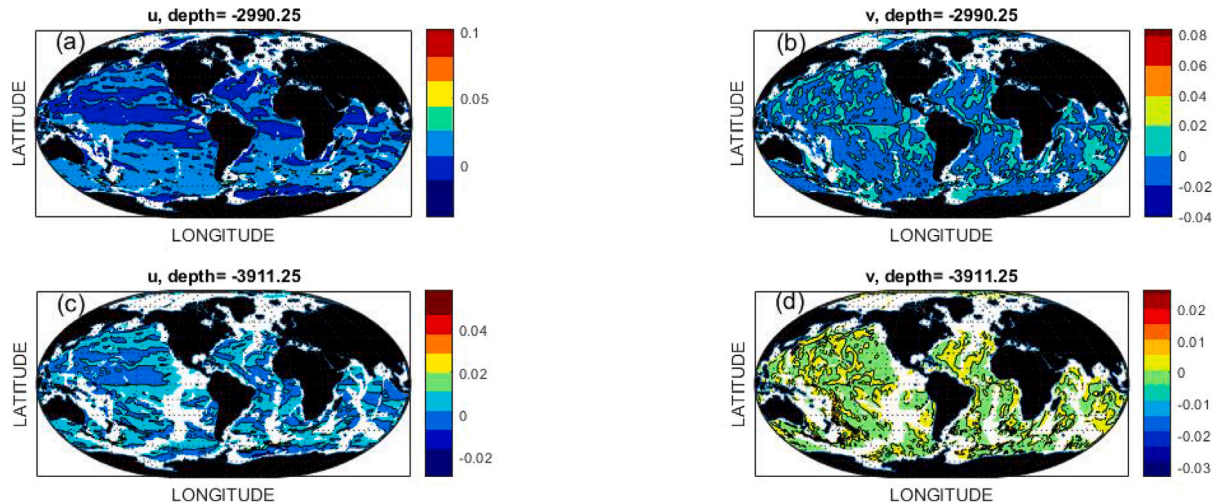

Fig. 2. Time-average zonal flow (left column) and meridional flow (right column) at depths of 3000 (a, b) and 4000 m (c,d).

w, from a shorter- in-duration ECCO estimate. The fields they found were strikingly complex spatially and with the vertical derivative of w, by implication, being even more so. If Eq. (1) is an accurate description, the corresponding spatial structures in v and its vertical derivative are expected. At 1000 m, apart from the Southern Ocean, little or no disturbance from the underlying topography is visually obvious. By 4000 m (Fig. 2c,d), topographic features (including mid-ocean ridges) and complicated lateral boundaries do intrude directly into the charts with the zonal flow taking on the more noisy elements seen above in v.

The highly structured flow fields at 4000 m (and extending some distance above—not shown) can be interpreted in terms of the complex bathymetry. Fig. A1 show the approximate topography used in the model. The gradient of h (not shown) is not simple to describe except that the topography on the grid-spacing is extremely rough with gradient magnitudes of less than 10^{-4} being very rare. In particular, truly flat bottom regions of the global ocean have a very limited spatial extent. Dynamical response to the variety of ridges, seamounts, abyssal hills, etc., will depend upon their shape, latitude, height, local stratification, and magnitudes and directions of any time-mean and time-variable flows. Each feature will also generate local boundary
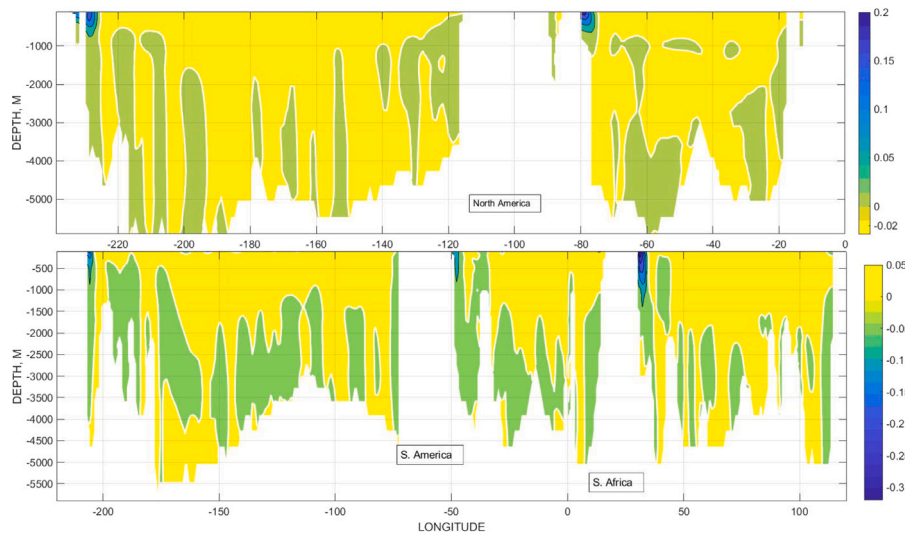
Fig. 3. Meridional velocity at 30°N (upper panel) and 30°S (lower panel) in m/s. Note that the longitude and color scales are different in the two panels and the colorbars reversed so that yellow-orange colors are regions of equatorward flow and thus of opposite sign to greenish areas. Even with 26 years of averaging, a highly structured but numerically weak meridional flow persists at all depths. An intense western boundary current near-surface is just visible in all oceans.
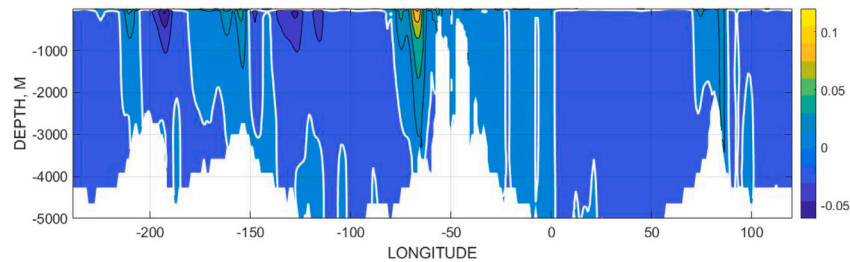

Fig. 4. Mean meridional velocity at 60°S. Zero contour is marked in white. Yellow-orange and light-blue regions here are equatorward flow (positive v). In contrast with mid-latitudes, a strong tendency to barotropic (uniform with depth) flow is conspicuous.

layers on the slopes (Losch and Heimbach, 2007, discuss some aspects of the topographic sensitivity of the general circulation.). The applicability of theories of flat-bottom oceans are questionable and conceivably theories encompassing two-dimensional stochastic topography are required (Radko, 2023, discusses many of the consequences of oceanic flow over topographic features.). Parallel considerations arise from the complicated lateral boundaries, with the effects of re-entrant corners, shelves and slopes, canyons, etc. persisting into the longest possible time-averages.

2.1. Velocity sections-meridional v

Consider first the meridional velocity across two latitude bands shown in Fig. 3. Characteristically, both show a v-component intensified in a near-surface western boundary current, and a very much weaker interior flow. The latter contains a sign-reversing columnar structure generally below about 1000 m, sometimes identifiable with local topography. Such lateral structures in the deep flow field have persisted for decades in the state estimate. What is perhaps surprising is the absence, except in the Southern Ocean and a few regions (Fig. 4), in the near-surface fields (above about 1000 m) of any obvious indication of the presence of such powerful flow and mixing disturbances as the mid-ocean ridges.

2.2. Velocity sections–zonal u

The character of the zonal velocity, u, orthogonal to the 165°W meridian in the Pacific, is shown in Fig. 5 and displays a rich variety of structures as does an Atlantic meridional section shown there. The

equatorial undercurrent is visible (smoothed by the contouring algorithm) in both sections. The only simple summary statement would be that the flows again remain highly structured after 26-years of averaging.

2.3. Meridional overturning circulation

The zonally integrated meridional transports have in recent years become the focus of interest as they represent a very great simplification of the flow field and, particularly, as they might directly reflect a changing climate system. Fig. 6 displays the zonal integrals of v in the northern hemisphere at 31°N for the sum of the Atlantic and Pacific Oceans and for the Atlantic alone. Both summations correspond to conventional expectations (e.g. Talley et al., 2011) with the global result showing northward time-average flow above about 1000 m and which includes both the Kuroshio and Gulf Stream. Below that, the southward flow consists of the intermediate waters and then a reversal reflecting the northward movement of Antarctic Bottom Water. The North Atlantic profile shows the dominance of the intermediate levels there by North Atlantic Deep Water, but with a much reduced injection, compared to the Pacific, of near-bottom Antarctic-origin waters. (See Roquet and Wunsch, 2022, for references and a commentary on the interpretations of the Atlantic portion).

Corresponding integrals for heat, freshwater, etc. are also readily computed but not shown here. Interpretation of such integrals raises awkward questions, analogous to those in W23, which concerned a one-dimensional physics, as to whether a two-dimensional representation of integrated transports across highly diverse flows has any easy interpretation? Results in Fig. 6 involve integrals across flow fields such as
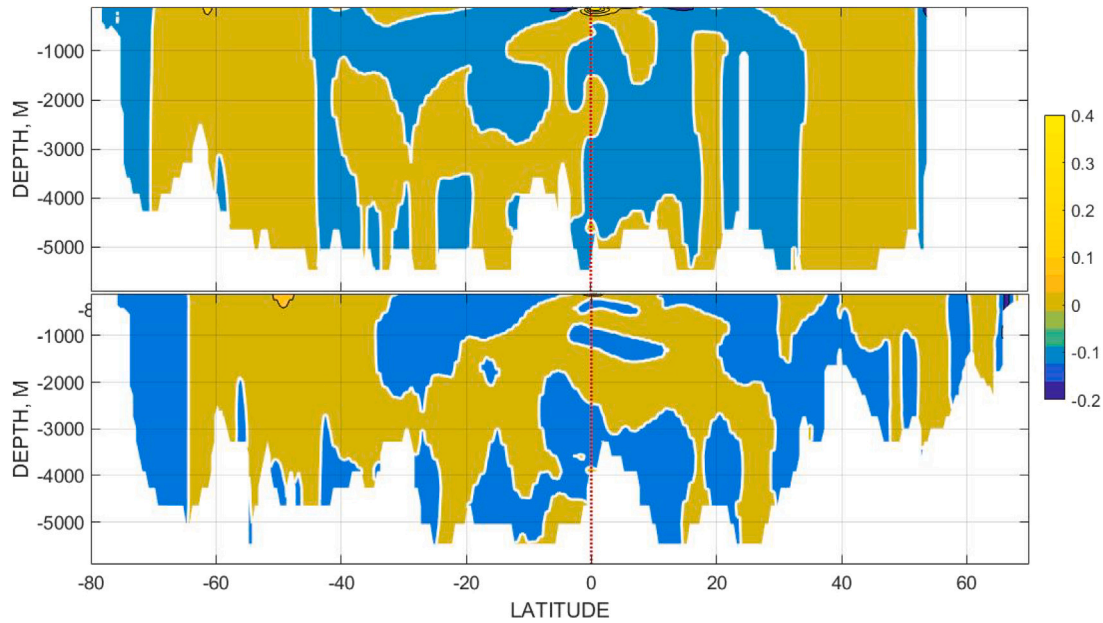
Fig. 5. Time-mean zonal flows along 165°W and 30°W. Latitude scales are identical in the two sections with the white contour denoting zero. Equator is marked by the vertical dashed line. Extended regions of depth independent flow appear.
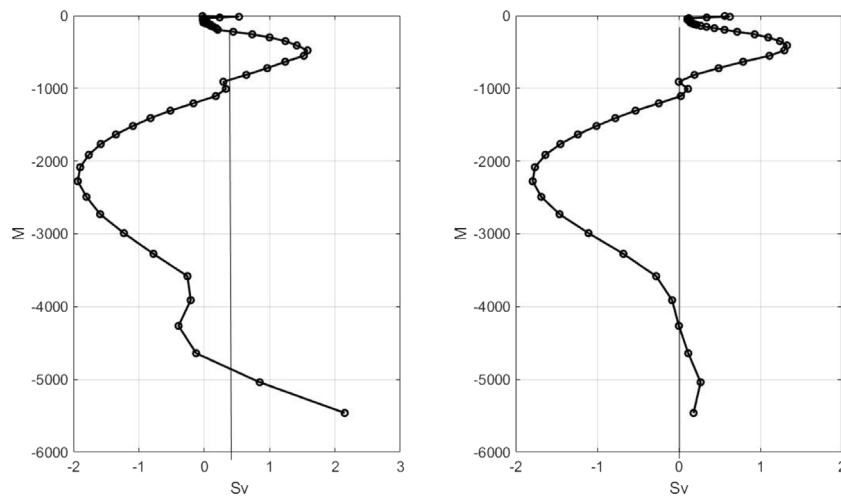

Fig. 6. Zonal integral of the time-averaged meridional velocity, $v(y, z)$, for the global ocean at 31°N (left-panel) and for the same latitude (right panel) in the North Atlantic alone. Both results correspond to conventional expectations.

those depicted in Figs. 3 where the velocity – and its underlying physics – varies greatly with longitude and depth.

2.4. Rossby number

The log (base 10) of the Rossby number, defined here as $Ro = \sqrt{u(x, y, z)^2 + v(x, y, z)^2} / f(y) L$ based upon a distance of $L = 1°$ of latitude is shown for two depths in Fig. A3 at 5 and 553 m. Apart from the expected singularity on the equator, the Rossby number is less than 0.1 everywhere, including the surface with exceptions in the Southern Ocean. Charts at greater depths (not shown) all produce smaller values. A robust inference is that the system overall is consistent with geostrophic balance, subject to the caveat that a small Rossby number is a necessary, but not a sufficient, requirement for that to be so (large Ekman numbers or equivalent could preclude the inference). A

general westward intensification appears in all oceans. Many *Ro* values in the Southern Ocean are O(0.1)—sufficiently large that nonlinear effects will not necessarily be negligible.

2.5. Some generalizations

From this preliminary sketch of the structure of the time-mean flow field, a few globally applicable generalizations appear possible. (1) The 26-year average field remains markedly structured, particularly in the abyss, where it is subject to strong topographic barriers and unresolved boundary layers. (2) The sub-tropical gyre structures emerge robustly in the two horizontal components of flow in the upper approximately 1000 m. (3) The three-dimensionality of the flow field precludes a simple explanation from a two-dimensional physics e.g., that as portrayed in Fig. 6. (4) The considerable remaining spatial structures leave
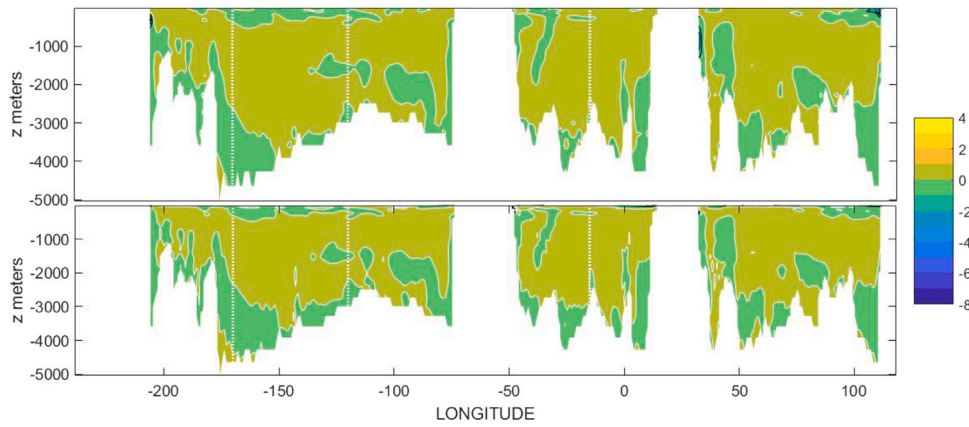
Fig. 7. Thermal wind shear (s^{-1}) from ρ (upper panel) and dv/dz (lower panel) directly from the estimate at 30°S both multiplied by 10^4. Topographic details appear to vary owing to the way in which $x-$ and a $z-$derivatives are taken in different directions relative to the various boundaries. Although the two fields differ in small values at depth, only the zero contour is readily visible, showing that the large-scale patterns are nearly identical.

several outstanding questions including: Which of them would persist in a much longer time average and which would be suppressed? Are any of them artifacts of the turbulence closure represented by the model?

3. Thermal wind

Theory (e.g., Pedlosky, 1982), and the small Rossby numbers seen in Fig. A3 suggest strongly that on the scales of the general circulation (vaguely defined, but here larger than the basic grid scale), geostrophic balance should be maintained almost everywhere. As already noted however, a small Rossby number does not preclude the effects of relatively strong dissipation or eddy fluxes of either sign. On scales smaller than those resolved here exceptions to large-scale geostrophic balance will arise from the effects of balanced eddies, the sub-mesoscale (see e.g., Garabato et al., 2022), along-stream pressure gradients in western boundary currents (WBCs), the numerous boundary layers near the sea-surface and near topographic features. With the partial exception of the WBCs, these regions are not resolved in ECCO(v4r4). Numerous textbooks discuss the expected geostrophic balance in the interior fluid through the applicability of the thermal wind equations, which are, in local Cartesian coordinates, (x, y, z),

$$f \frac{\partial v}{\partial z} = -\frac{g}{\rho_0} \frac{\partial \rho}{\partial x}, \tag{2a}$$

$$f \frac{\partial u}{\partial z} = \frac{g}{\rho_0} \frac{\partial \rho}{\partial y}, \tag{2b}$$

representing the vertical shear in terms of the horizontal density gradients. f and ρ are the conventional Coriolis parameter and the in situ density. ρ_0 is a constant reference value. Historically, these equations were used with observed hydrographic fields in finite difference form to find the horizontal flow field up to an unknown integration constant. A scale analysis (see e.g., Phillips, 1963; Pedlosky, 1982) shows that this balance is the expected one, apart from boundary layers (including those at the surface and on sea-floor topography and side-walls) and on and near the equator where $f \approx 0$ and, evidently, in much of the Southern Ocean. Separate discussion of the meridional and zonal geostrophic velocities is both convenient and necessary as will be seen.

3.1. Meridional thermal wind

In the meridional component, the thermal wind shear involves a horizontal (in x) derivative of ρ, and the corresponding vertical shear of the velocity field in the state estimate requires a vertical derivative of the northward velocity component v. Anywhere adjacent to a topographic feature, disagreement is expected between the thermal wind shear and $\partial v/\partial z$ both because unresolved boundary layers of several

types are anticipated there, and from the simple centered finite differences being used here. These differences render visual topographic details differently. As will be seen however, over the great bulk of the ocean, quantitative agreement is found. In practice, use of simple centered-differences appears to produce as much similarity between the two fields as does use of the differencing stencil of the model (not shown).

Consider first a single zonal section at 30°S (Fig. 7) spanning all longitudes, some of which are land. Visually, the two patterns of the two sides of the thermal wind equation differ in small details, many being attributable to the finite differences taken in the presence of complicated topographic boundaries. The median difference is 2×10^{-7}/s. Vertical profiles of the thermal wind shear (computed from ρ) and $\partial v/\partial z$ at three longitudes are displayed in Fig. 8. A comparable display for 60°S is in Fig. A6—and showing a greater visual difference between the two calculations.

To obtain a quantitative measure of the degree of similarity of the two fields, consider at each horizontal point the two vectors in z_j corresponding to the discrete rendering of $\mathbf{a} = \partial v (x, y, z_j) / \partial z$ and $\mathbf{b} = g/(f \rho_0) \partial \rho (x, y, z_j) / \partial x$. The projection $p_v = \mathbf{a} \cdot \mathbf{b} / (|\mathbf{a}| |\mathbf{b}|)$ is the cross-correlation of the vertical structures of the thermal wind shear and the vertical derivative of v in the model. But as the system is here being treated as deterministic (probability densities for the spatial structures are not available), the outcome of the numerical cross-correlations will be referred to as the "normalized projection" of the two fields (or just the " projection") with maximum magnitude 1. From the figures, including e.g. Figs. A5, A7, a variety of deviations in the upper few hundred meters are apparent and the projections are taken below 200 m.

The magnitudes (all positive) of p_v are shown in Fig. 9 and generally exceed a value of 0.8. Reduced values occur where anticipated—including boundary regions on the African coast and elsewhere, high northern convective regions of the North Atlantic, the Kuroshio extension, and in the Southern Ocean and the southern hemisphere generally. Regions of deviation from large-projections are generally the result of failure of the thermal wind balance in the near-surface (down to about 200 m), as can be seen in Figs. 8, A5.

Thermal wind balance of the meridional flow, v, appears to be a good general oceanic description with the exception of the equator and parts of the Southern Ocean – both regions where a failure would be expected from the basic physics of the vanishing of f in the former, and in the latter of the ageostrophic components of the topographic pressure balances in quasi-zonal flows. Behavior in the Southern Ocean is interesting – and the physics there has been the subject of much discussion (see e.g., Wolfe and Cessi (2010), Vallis (2017) Wilson et al. (2022) and their numerous references). Adjacent to topography, the situation
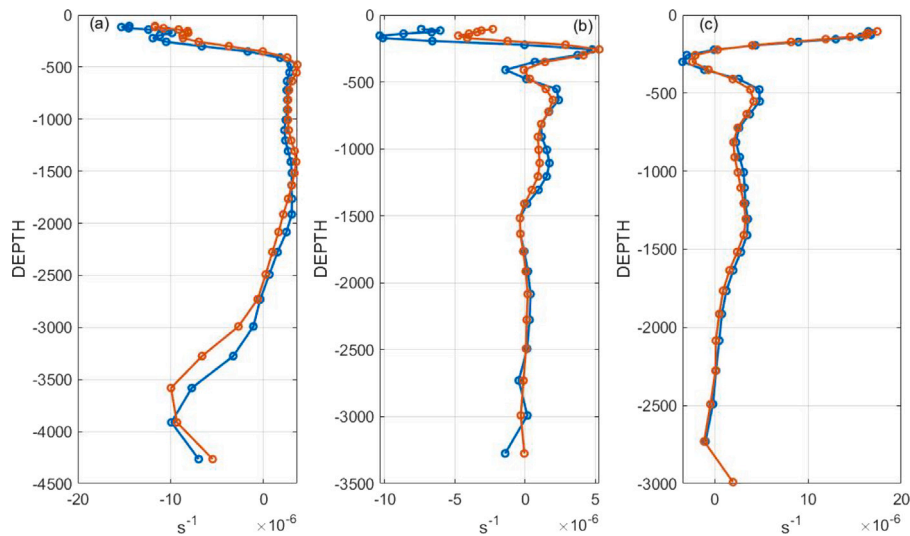
Fig. 8. Profiles with depth of the thermal wind shear (blue) and of $\partial v/\partial z$ (red) at three Pacific longitudes 170°W, 120°W, −15°W at 30°S. Shallowest point is at 100 m.
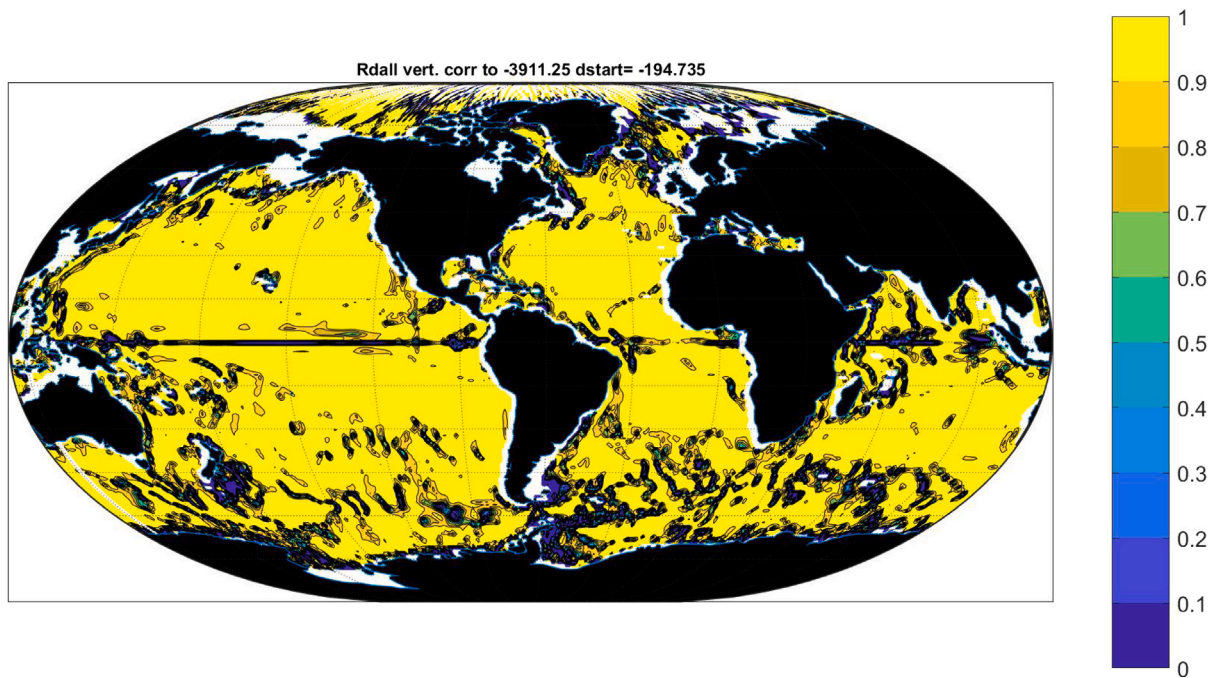

Fig. 9. Global values of the projection, p_v, of the vertical structure of the meridional thermal wind shear onto the vertical shear, dv/dz from 200 m depth downward to 4000 m. Apart from the Southern Ocean generally and the immediate vicinity of the equator, the two fields are similar.

is somewhat obscure, as both a failure of boundary layer resolution, and numerical issues of differentiation of topographic, partially filled, grid boxes occur.

3.2. Meridional lines–zonal thermal wind

Local thermal wind-shear balance is more fragile in the zonal flow, u, than it is in the meridional component, v. The literature on zonal jet formation suggests a much greater sensitivity of zonal mean flows to the eddy field than is the meridional component. A strong tendency toward zonal flows occurs, especially in the Pacific Ocean, both in the variability (not shown) and time-averages of varying duration. See for example, Berloff et al. (2009) or Chen et al. (2015); both are idealized analyses of turbulent interactions and divergences leading to zonal jets. The edited volume by Galperin and Read (2019) discusses the subject in the wider context including the atmospheres of both of the Earth and

of the giant planets. Oceanic zonal flows are potentially generated by a variety of detailed turbulent mechanisms and interactions with the background velocities.

In a dissipationless ocean without meridional barriers, zonal flows are free solutions and will also tend to appear if western and eastern boundary currents can absorb or provide the incoming or outgoing flow. To the extent that deviations from geostrophic balance occur in the present state estimate, they would arise from the parameterizations used to represent the unresolved eddy fields and boundary layers. Fig. 10 displays the zonal thermal wind shear and $\partial u/\partial z$ along 165°W. Profiles of the two fields at three latitudes along this longitude are in Fig. 11. Because of the equatorial singularity, $f\,\partial u/\partial z$ is computed from Eqs. (2). The two fields range from showing near-coincidence to considerable differences. Projections will, in any case, be dominated by the upper 500 m where the shear is greatest.
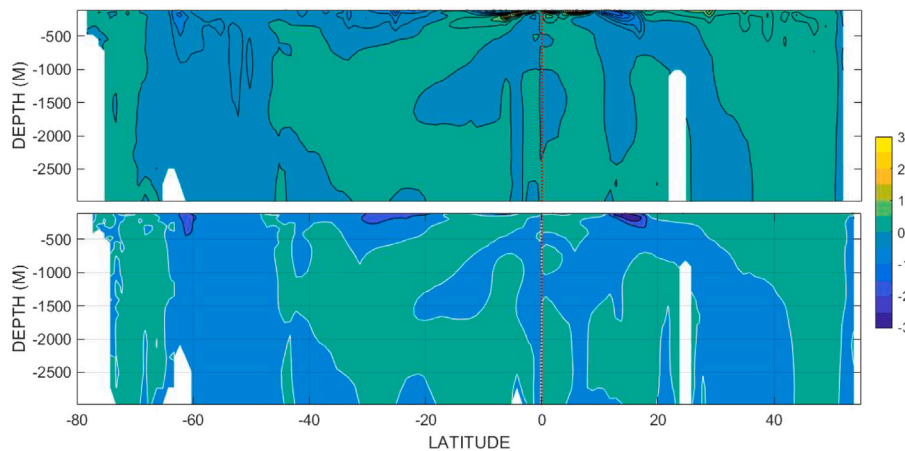
Fig. 10. Upper panel is f times the thermal wind shear along 165°W and lower panel is the corresponding vertical derivative of the model $u(x, y, z)$ *starting at* 100 m. As with the meridional flow, only the zero contour is obvious with the sign changes at depth being nearly identical. Qualitatively great similarity is apparent but with small systematic offsets in the deep water.
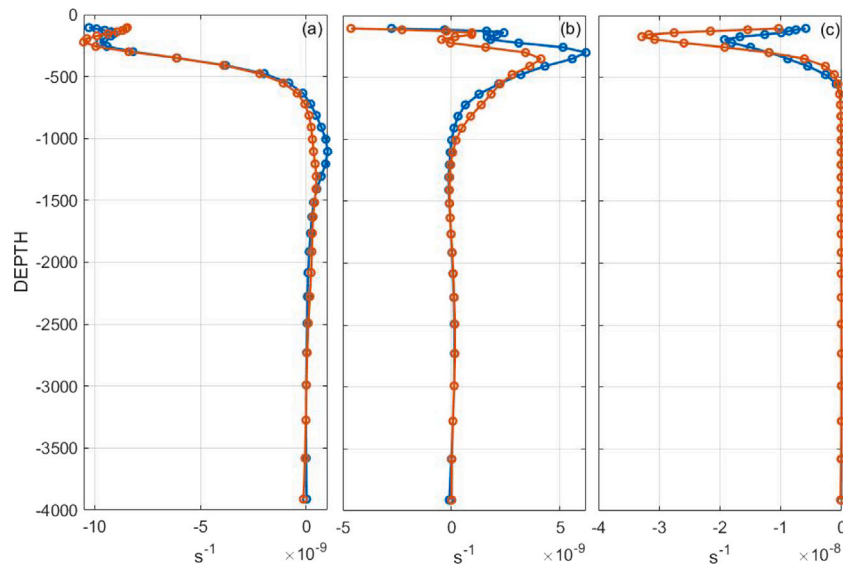

Fig. 11. Profiles of thermal wind shear (blue) and $\partial u / \partial z$ (red) along 165°W. From left to right at 30°W, 15°W, 15°E. Strongest deviations between them tend to occur above about 1000 m depth. Other profiles can be found in Appendix.

Apparent regional deviations from thermal wind shear as an accurate determinant of $\partial u / \partial z$ can arise from at least two causes: (1) low-frequency time-variation in a particular area renders the temporal average relatively far from a true value. (2) Strong unresolved eddy divergence effects are present, rendered in the state estimate through the parameterized values. Spectra of low-frequency variability is likely different for u, ρ. Fig. A2 shows the logarithm of the annual standard deviation for surface speed computed from the annual averages in the surface layer about the 26-year mean for each grid point and which produces, as is well-known, a very strong regional dependence.

A global chart of the profile projections, p_u, is in Fig. 12. In contrast to Fig. 9, the result displays a series of dominantly zonal bands of reduced projection values. The summary statement might be that although thermal wind balance of the zonal flow is a good approximation over much of the ocean outside the Southern Ocean, regions of measurable deviation do exist with a dominantly zonal character at mid- and low-latitudes. How much of the structures shown in the global projection maps will survive different closure schemes and much higher model resolution remains an imponderable.

3.3. f/h contours

One of the robust implications of a steady geostrophic flow over large-scale topography is that the streamlines should follow the contours of f/h (e.g. Vallis, 2017). With the realistic complicated topography, $h(x, y)$, (see Fig. A1) much regional structure exists. The extent to which even apparent abyssal planes are free of hills and other low-level disturbances and have no detectable effect on the boundary layers and overlying water-column is not obvious. Applicability of this particular physics may be greatly restricted. One example of an exception, noticed long ago, is the small region of closed contours in the Argentine basin. de Miranda et al. (1999) discuss studies of what is called the Zapiola Drift. Note the intensified flow there in e.g., Fig. 1(c-f).

3.4. Reference levels

In the era of ship-borne oceanography, the only general circulation estimates that could be made used the thermal wind shear—converted to absolute velocity by assuming a deep "level-of-no-(horizontal) motion", or "reference level." Recent observational tools produce direct
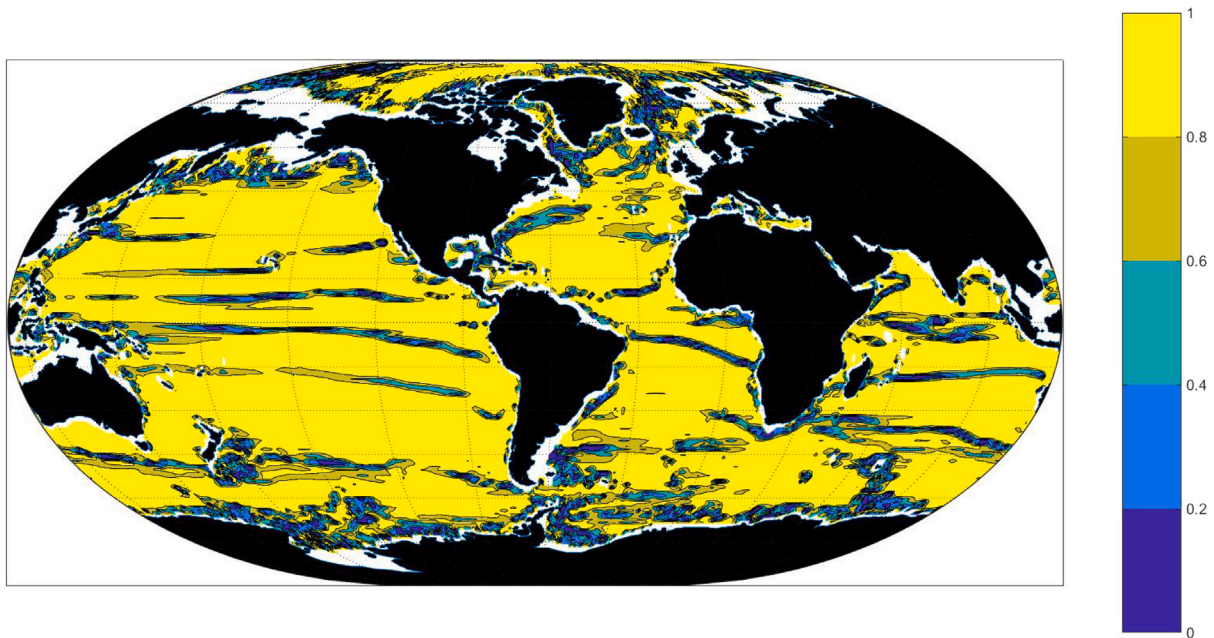
Fig. 12. Projection, below 200 m of the zonal component of thermal wind shear profiles, onto the profiles of $f\,\partial u/\partial z$ directly from the state estimate. Note the zonally-banded structure here is mostly absent in the meridional flow component. Numerous reduced values contrast with the results for the meridional vertical shear.

estimates of absolute values of u, v (altimeters, floats, improved meteorology combined with higher order dynamics, . . .) and a historical question is whether some simple distribution exists for levels of minimum speed and/or velocity components?

Whether the result from the 26-year average, showing the depth of minimum flow is simple is a matter of taste. Even when smoothed over 10° degrees of longitude and 5° of latitude, or summed over longitude, the result for the net speed (Fig. 13) has much structure. A gross generalization is that minimum speed depths in the tropics tend to lie between 500 and 1000 m, and at high southern latitudes, are generally close to the seafloor, but with numerous exceptions. Even the zonal averages in water depths exceeding 3000 m (Fig. 13) are not simple. In the North Atlantic reference levels-of-no-motion for v have commonly been chosen near 1500 m (e.g., Leetmaa et al., 1977) and these present results suggest a value of smallest speed nearer 2000 m there.

4. Spirals

Velocity spirals enter into discussions of oceanic flow under at least three circumstances: (1) in the Ekman (1905) layer; (2) in large-scale geostrophic flows as the beta-spiral (Stommel and Schott, 1977); (3) the surface manifestation in the submesoscales of Munk et al. (2000). For present purposes, (3) is not relevant. The question of the extent to which the time-averaged state estimate is at least consistent with either of the remaining descriptions is worth asking in the pursuit of global-scale descriptors (An apparent Lagrangian particle spiral in the Southern Ocean has been described by (Tamsitt et al., 2017), but the discussion here is confined to Eulerian mean values.).

4.1. Near-surface Ekman-like spirals

The ECCO(v4r4) model lacks the near-surface resolution required to depict the complex processes, including the energetically dominant surface waves, Langmuir cells, Stokes velocities, seasonal and night-time convection, and other flows present in and near the upper boundary of the ocean. The literature, dating back to 1905 and Ekman's paper, postulates the existence of an Ekman layer in an unstratified, uniformly rotating fluid. Price et al. (1987) discuss observations and realism

issues. In a notation almost identical to theirs, the classical Ekman layer takes the form,

$$[u(z'), v(z')] = V_0 \exp(-z'/D_E)\left[\cos(\pi/4 - z'/D_E), \sin(\pi/4 - z'/D_E)\right]$$

(3)

$$V_0 = \frac{\tau}{\rho_0 (A_v f)^{1/2}}, \quad D_E = \left(\frac{2A_v}{f}\right)^{1/2}$$

where τ is the mean wind-stress, however defined, A_v is a vertical eddy viscosity, and D_E is the Ekman depth. At $z' = 0$ $(u(z'), v(z'))$ lie at 45° to the right or left (northern/southern hemisphere) of the resting sea surface. Some of the consequences of stratification and heating are described by Price et al. (1986) and by later authors. With the ECCO layer thicknesses of 10 meters between the surface and 100 m, resolution of a classical Ekman layer is possible (Price et al., 1987). McWilliams et al. (2012) analyze numerically some of the complex, intense, surface wave and Langmuir circulation effects, and Shrira and Almelah (2020) discuss some consequences of time-dependent viscosity/dissipation. The ECCO near-surface boundary layer model is based on that of Gaspar et al. (1990) and which includes stratification. These papers and numerous related ones mean that finding a useful wide-spread description of the expected upper-level current structure in the mean-state is not necessarily possible.

Perhaps surprisingly, near-surface spirals are found in the ECCO(v4r4) time-average—spirals whose hemispheric dependence on the sign of the Coriolis frequency is consistent with that expected for the simplest Ekman layer of an unstratified, otherwise resting, ocean.

Consider first Fig. 14 that shows hodograph plots with depth z at four locations along the 165°W meridian. A typical behavior is the change from Fig. 14(a) of a counter-clockwise spiral to a clockwise one across the equator in (c,d). The spiral construct fails at a distance of 1/4° from the equator—the nearest grid points. Note that in panels (a), (c) the top layer (5 m thick) does *not* reproduce the classical Ekman layer result having a maximum speed at the surface, whereas (d) does show that result.

A simple test of a spiral-like behavior is used here by computing the sign of the turning with depth in the hodograph at each lateral grid point. Ekman-like behavior appears, producing a counter-clockwise
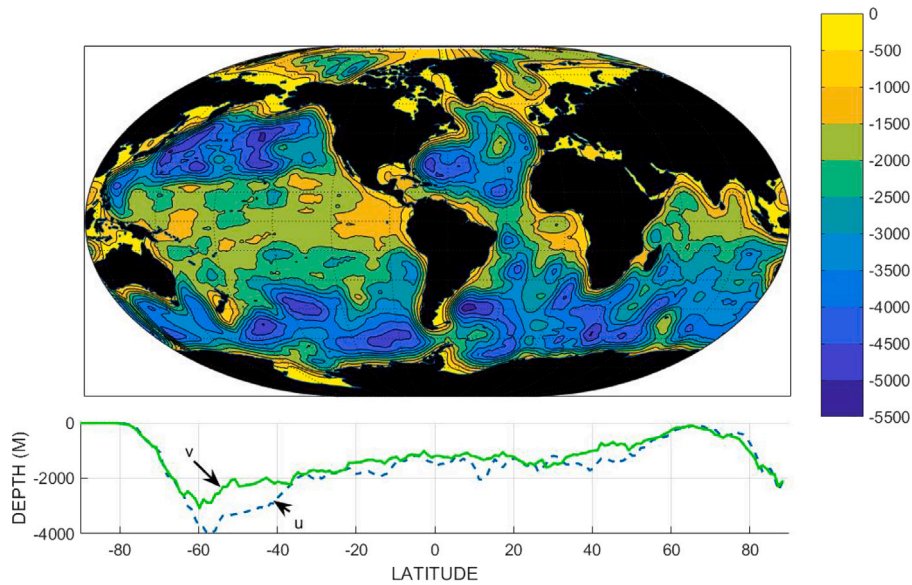
Fig. 13. (Map, upper panel) Depth of the minimum speed in the water column, where the depth exceeds 3000 m. Values were smoothed over 10 degrees of longitude and 5 degrees of latitude. Tropical and high latitudes do differ but each band has numerous structures. (Lower panel) Global zonal average of the depth of minimum flow shown for u, v separately.
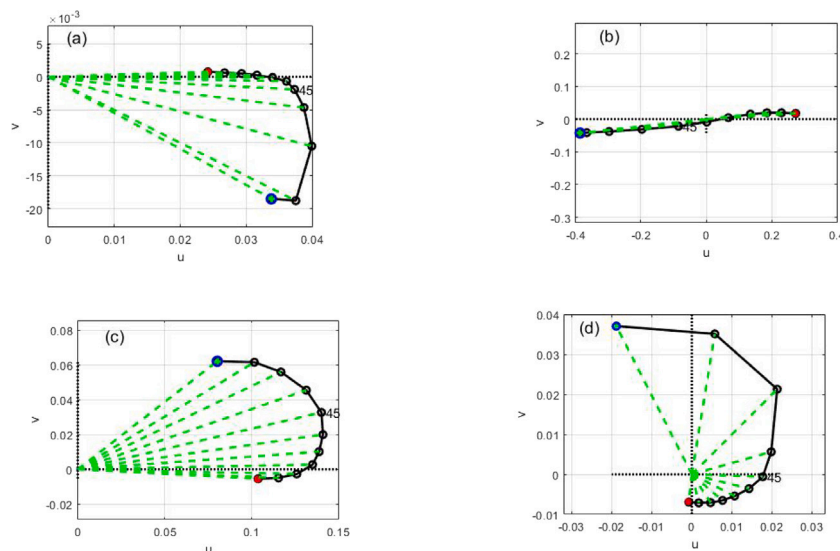

Fig. 14. Sample hodographs along 165°W in the central Pacific Ocean at different latitudes. Units are m/s. Blue dot denotes the value (5 m layer) nearest the surface, and the red dot the terminal value at a depth of 105 m. 45 m depth is marked. South of the equator (a), movement is counter-clockwise with depth (here the velocity magnitude is largest in layer 2). (b) Hodograph at 0.25°S showing the expected failure of a simple Ekman-like spiral on and near the equator. (c,d) show clockwise spirals in the northern hemisphere at 4.75°N and 19.75°N. (c) has a clear spiral, but one of increasing magnitude with depth down to about 50 m. (d) Spiral has the property that the top layer has the strongest flow.

spiral in the Southern Hemisphere (increasing, positive angular sign with depth), and a clockwise spiral (increasingly negative sign angle sign with depth). A measure of consistency – quality of the fit – within the upper layers is computed from the sign of the change from one layer to the next in the 5 layers (Fig. 15). A value of ± 1 means complete consistency (spiraling at all depths with a surface maximum), and a value of $\pm 1/2$ implies a single reversal between two of the layers, but with an overall consistently spiral-like behavior. The most common cause of a reduced magnitude quality value is the occurrence of the maximum in layer 2 rather than in the top-most layer (as seen in Fig. 14a,c). Nonetheless, the spiral structure remains. With some minor regional inconsistencies, generally near boundaries and including parts of the Mediterranean, the expected different signs in the two hemispheres is pronounced. Generally speaking, the fit is best far from oceanic boundaries. That the underlying physics is Ekman-like is a reasonable

inference, albeit the behavior of the underlying turbulence remains to be understood and further exploration involves the vector wind-field and buoyancy forcing.

The estimated e-folding scale depth, D_E, is determined from a least-squares fit to the logarithm of the hodograph from Eq. (3) analogous to the procedure in W23. The fit was made for layers 2–10. Compared to the sense of rotation, it is less spatially stable, even with a time average. Again the question arises of whether a 26-year average is of sufficient duration to provide a stable mean? The physics may well be that of an Ekman layer—but here it is just a readily computed reparameterization of the flows in the uppermost layers. Fig. A4 displays the equivalent value of A_v determined from D_E although its significance remains obscure and the result is spatially very variable. To the extent the physics is indeed that of Ekman layers, the corresponding patterns of
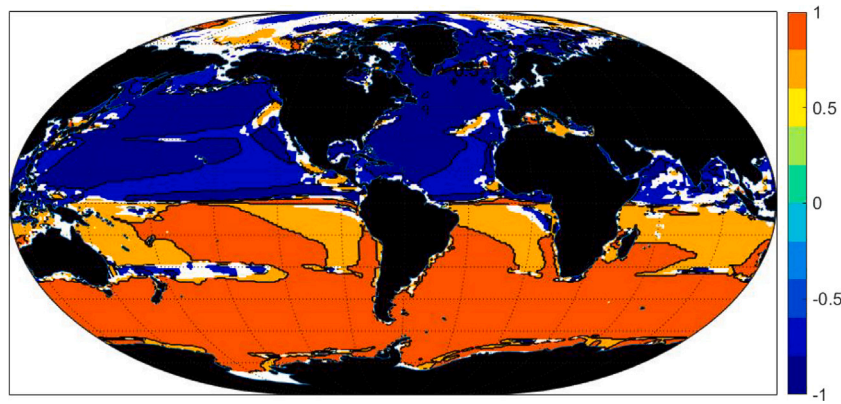
Fig. 15. Orange-red regions display a counter-clockwise behavior in the flow of the surface layers, and the blue areas are correspondingly clockwise, both as expected from Ekman-like dynamics with a sharp change across the equator. Values represent a measure of the quality of the spiral fit in layer 2 and below. Darker colors indicate a stronger fit. Those less than |1| exhibit some inconsistencies, but spiral direction is, overall, as indicated by the sign. Blank regions of failure are associated with eastern boundaries and quasi-zonal bands, especially east of Australia.

injection of wind energy to the circulation are discussed by Roquet et al. (2011) for an earlier ECCO release.

4.2. Beta-spiral

The expected turning of the time-averaged flow with depth in the geostrophically balanced interior was explicitly introduced by Stommel and Schott (1977) and elaborated in several later papers e.g., by Mc-Dougall (1995) for the presence of lateral mixing. For present purposes, the discussion in Olbers et al. (2012), P. 153+) of the formulation in geographic coordinates is adequate.[2]

In a perfect fluid in steady-state, conservation of density can be written,

$$u\frac{\partial \rho}{\partial x} + v\frac{\partial \rho}{\partial y} = -w\frac{\partial \rho}{\partial z}, \tag{4}$$

and with conservation of planetary potential vorticity leads (Olbers et al., 2012, their Eq. 5.67) to,

$$u\frac{\partial}{\partial z}\left(\frac{\partial \rho/\partial x}{\partial \rho/\partial z}\right) + v\left[\frac{\partial}{\partial z}\left(\frac{\partial \rho/\partial y}{\partial \rho/\partial z}\right) + \frac{\beta}{f}\right] = 0 \tag{5}$$

and which perhaps carries to its outer limit the present requirement of a "simple" relationship. Stommel and Schott (1977) produce a construct (their equation 1.4) for the rate of turning of the hodograph angle θ with depth as,

$$\frac{\partial \theta}{\partial z} = \frac{g}{f\rho\left(u^2 + v^2\right)}\left(w\frac{\partial \rho}{\partial z} - \frac{\partial \rho}{\partial t}\right) \tag{6}$$

for a perfectly geostrophic flow. $\partial \rho/\partial z < 0$ for static stability and, by assumption, the time-derivative of ρ vanishes in the time-average. Thus the sign of w determines the direction of turning. As long as a meridional component exists, the linear vorticity conservation equation (Eq. (1)) implies w is non-zero. Results in Liang et al. (2017) show a very noisy $\partial w/\partial z$.

Instead of attempting to determine the predicted rate of turning from Eq. (6), the simple question is asked whether evidence exists for interior spirals approximately encompassing the main thermocline? The answer to this question is "no": spirals do exist in many places (Fig. 16), but many others display a depth dependence closer to a straight line and others have no readily discernable analytic structure. Attempts to fit spirals over a depth range of 550 to 3000 m produced

a complicated spatial dependence (Fig. 16). Deviations from a simple spiral are expected from complexities in w, vertical changes in lateral kinetic energy, along with any generic deviation from perfect geostrophic balance.

The β−spiral thus does not produce any simple generalization about the flow field. A significant fraction of the ocean, but mainly in the Southern Ocean, exhibits a linear trend of the hodograph with depth, with the sign of the linear trend varying rapidly (not shown).

5. Where are the thermocline and pycnocline?

A centerpiece of dynamical oceanography is the theoretical explanation of the "main thermocline" in the upper ocean where the vertical temperature derivative is strongest, usually corresponding to maximum derivatives in salinity and density as well. That structure is normally distinguished from the seasonal thermocline which waxes and wanes over the year (see Talley et al., 2011). In the wider literature, definitions of the thermocline depth are vague—being replaced by various theories in different models and producing depths of the order of several hundred to about 1000 m (see for example, Pedlosky, 1996; Huang, 2010). A useful question is whether *a* thermocline depth can be defined in a time-average ocean?

The gist of W23 however, is the implication that temperature and salinity distributions can be very different—largely as a result of distinct boundary conditions at the ocean top and bottom, and the three-dimensional flow field. As discussed in the various thermocline theories, the dynamically important physics of the circulation lies with the density distribution and not with T, S separately. For that reason, only the geographical structure of the *pycnocline* in the time-average is depicted here.

Consider as examples Figs. 17, 18 for $\partial \rho/\partial z$ along 30°S, 30°N across all ocean basins. Visually, it is not easy to define a particular vertical scale characterizing the vertical rate of change. Generally speaking, vertical rates of change of density are largest in the region above 100m—usually considered the domain of the seasonal thermocline and of the Ekman and other boundary-layers. Evidently, the averaging process leaves a time-mean near-surface thermocline, interpretable as owing to the net fluxes of heat, moisture, energy, vorticity, and momentum. In the regions below 100 m, a general, near-exponential decline in the derivative occurs, but a single, ocean-wide characteristic depth is not visually obvious.

6. Discussion

From a focus on the flow field, the quest for universal, simple, properties and patterns in an estimated 26-year time-mean global

---

[2] In this context, the equations are usually written in terms of isopycnal or neutral surface coordinates instead of the z coordinate, but the latter is more stable in a geographical-coordinate model output.
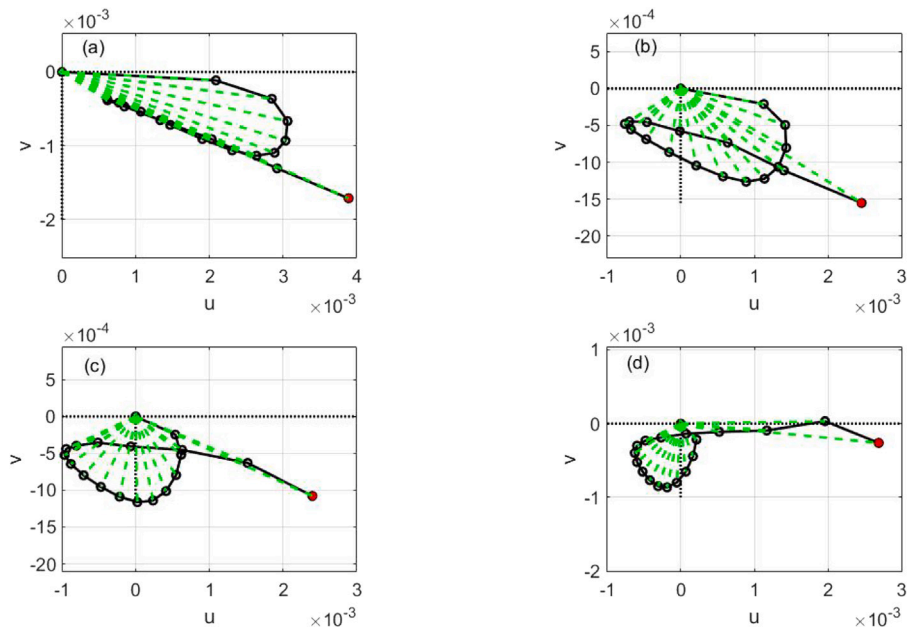
Fig. 16. Beta-spiral hodograph plots showing a variety of linear and spiral-like features along 165°W. Origin value is at 0,0 and ending depth is in red. Latitudes are 25°S, 0°,5°N, 20°N in panels (a) to (d). Depth range is 550 to 3000 m.
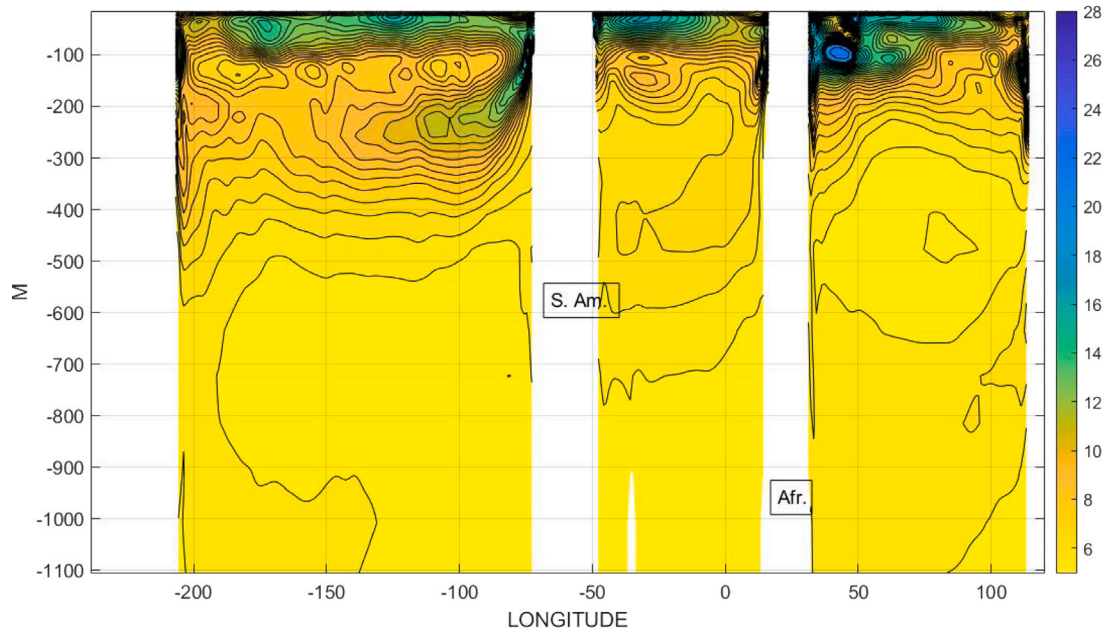

Fig. 17. 10^3 times $\partial\rho/\partial z$ at 30°S. The sign is rendered so that the derivative is positive downward. Contour separation is numerically constant. Density is the in situ value.

ocean circulation produces a number of results that characterize this specific time-average circulation and provide a basis, both qualitative and quantitative, for comparison with any other estimate of a time-average. The search for simplicity of description is satisfied only in part. A major, overall, description is the survival of much structure, particularly in the horizontal, despite the multi-decadal averaging time. Whether much longer, hypothetical, averaging times would produce any further great simplification remains unknown. Some properties and patterns nonetheless do emerge: (1) Over the abyssal ocean, an exponential fit in z to the potential density field is found (W23 and Rogers et al., 2023) and slowly varying with horizontal position scale height. (2) Apart from the equatorial region, the Rossby number based

on a 110 km scale, is small—less than about 0.1 everywhere. (3) Consistent with small Rossby number (a necessary but not sufficient condition), the meridional thermal wind shear is in geostrophic balance over most of the water column below about 200 m, with the Southern Ocean displaying apparent ageostrophic results above about 500 m. Zonal-flow thermal wind balance tends to be violated at greater depths in zonal bands. (4) Near-surface, and consistent with the implications of Ekman layers, spirals of clockwise (northern hemisphere) and counter-clockwise (southern hemisphere) turning with depth are found almost everywhere (Fig. 15), although departures from a strict surface max-imum flow do exist widely and the vertical scale height is spatially variable. (5) A single simple definition of the thermocline/pycnocline
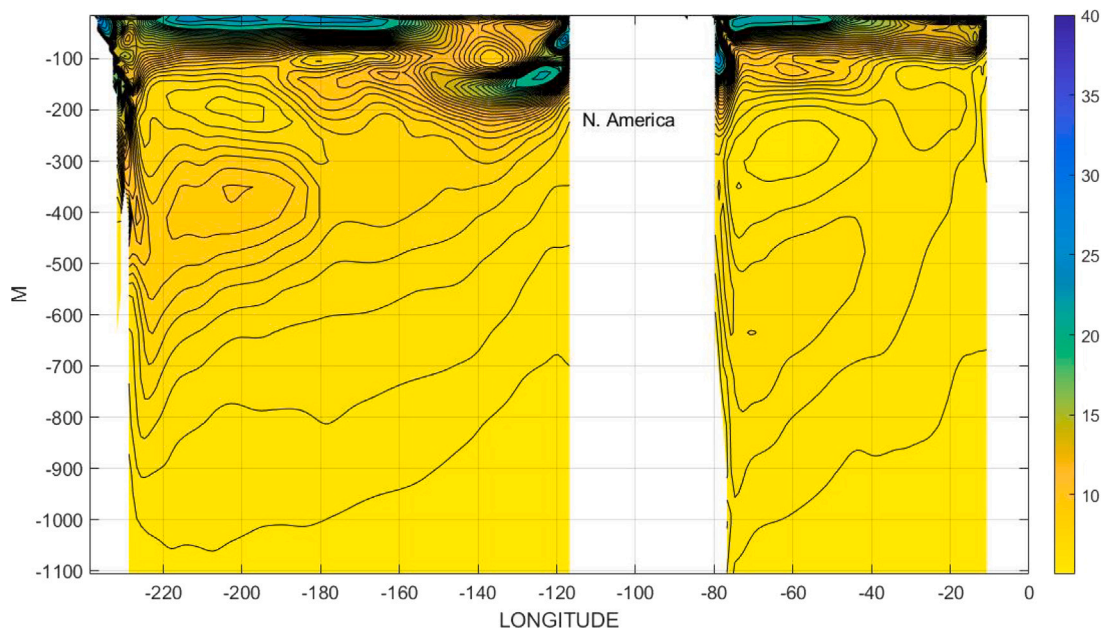
Fig. 18. 10^3 times the z derivative of in situ density at 30°N. The sign is rendered so that the derivative is positive downward.

Table A.1
Depths (meters) of the layers in the ECCO(v4r4) state estimate.

5	15	25	35	45	55	65	75	85	95	105	116	127	140	154	172	195	223
257	300	351	410	477	553	635	722	814	910	1007	1106	1206	1306	1409	1517	1634	1765
1914	2084	2276	2491	2729	2990	3274	3581	3911	4264	4640	5039	5461	5906				

depth is not obvious. (6) The issue of the dynamical equations governing the time-average circulation can be answered partially as being those for quasi-geostrophy in the meridional velocity except for the Southern Ocean and in the zonal velocity too with the addition of a number of quasi-zonal strips where deviations from balance exist. (7) The tentative answer to the question of whether spatial and temporal averaging are interchangeable (a hypothesis of simplification) is apparently negative, with the spatially complex influence of the sidewall and bottom topography boundaries emerging as strong signals in the time-average. Any hope that a multi-decadal average would produce a simplified ocean circulation is only partially borne out.

Many interesting descriptive extensions of this work will be obvious (e.g., Buzzicotti et al., 2023, focus on spatial scales of the kinetic energy). Diverse regional variations exist and other global fields such as the potential vorticity, or energy transports can be investigated. The temporal variability underlying this time-average requires extended discussion by region, frequency, and wavenumber.

A final caveat to all of the above is that the ECCO(v4r4) state estimate is indeed only an *estimate* of the ocean circulation—albeit one that largely fits the global scale data constraints of the open ocean (listed in various of the references), and simultaneously is a full solution to a consequently adjusted, free-running, oceanic GCM. An old rule-of-thumb for analysis of time-series is that recalculation is worthwhile when the duration doubles in length. The present time-estimate will grow incrementally with the passage of time assuming the existing observational networks are sustained. But in the interim, the model should improve, resolution should increase, and more data will be better understood. Ultimately however, the fundamental question facing anyone using existing ocean models underlies all of the results here: To what extent does a coarse resolution model, regarded as a generalized turbulence closure, produce a faithful representation of the global scale, three-dimensional fluid? The "closure" includes numerous assumptions, of which the eddy parameterizations are the most apparent, but including the unresolved boundary layers at the bottom and lateral boundaries.

Credit authorship contribution statement

Carl Wunsch: Conceptualization, Formal analysis, Methodology, Software, Writing – original draft, Writing – review & editing.

Declaration of competing interest

I have no competing interests

Data availability

Data Availability Observational data were used only indirectly this paper. The ECCO state estimate as well as the underlying model and the observational data used for it can be found on the ECCO JPL/NASA website: https://ecco.jpl.nasa.gov/drive/files/Version4/Release4.
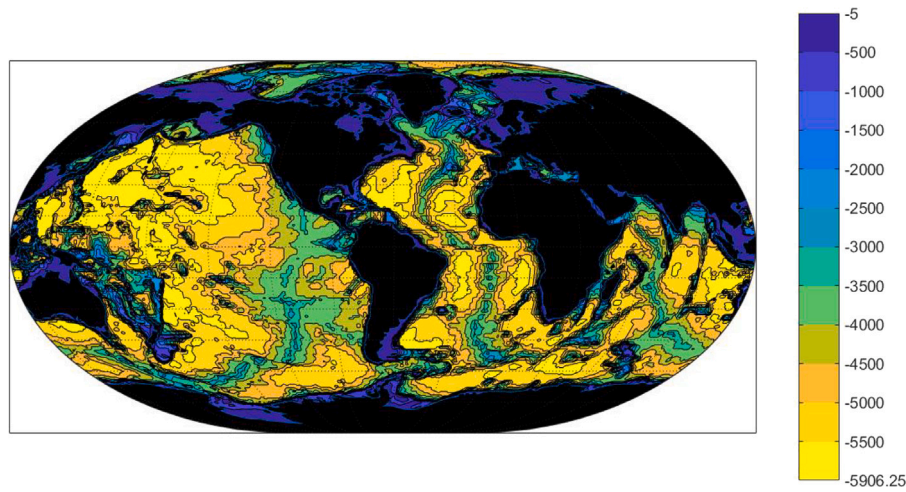
Acknowledgments

Fig. A1. Bathymetry, h, used in the state estimate model. Depths in meters. Layer depths are listed in Table A.1. The complexity affects the flow field out to the longest time-scales. Those features will not disappear with temporal averaging. Note that detailed observations of global topography remain incomplete (DeSanto and Sandwell, 2019). Very small-scale roughness is likely important in the overall circulation.
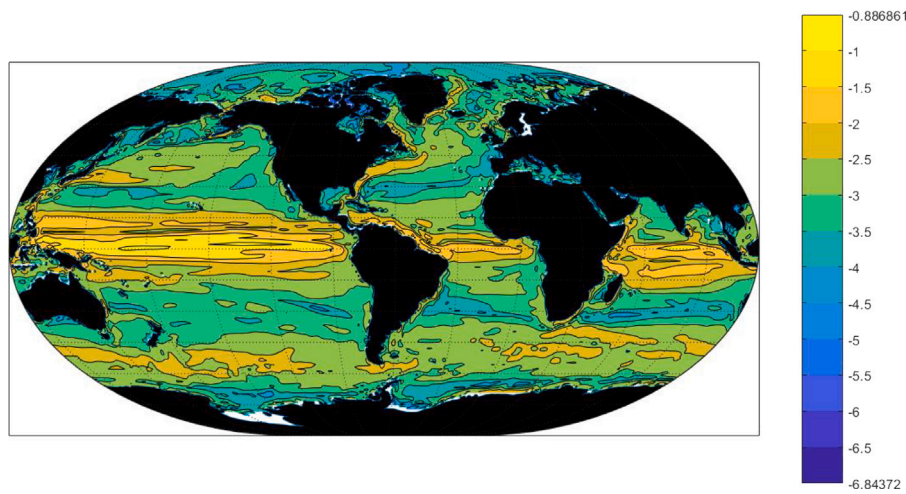

Fig. A2. Logarithm of the standard deviation of surface speed, m/s, based upon variations in 26 1-year averages. High latitudes are conspicuously noisy, in the sense of having large temporal deviations, with maxima apparent e.g., in the Kuroshio and Gulf Stream extensions. The tropics, with their short-time scales of variability, are obvious. Column total patterns are similar but with relatively larger values in the Southern Ocean. Quasi-zonal bands of low and high variance are conspicuous.
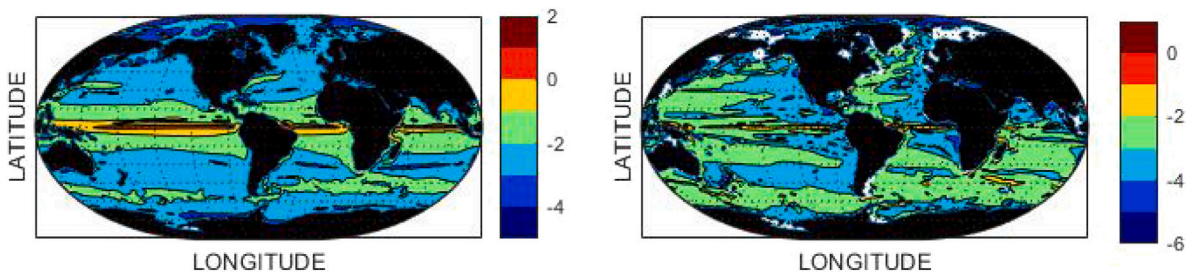

Fig. A3. Log_{10}(Rossby number) at 5 m (left panel) and at 550 m (right panel).

Appendix. Topography, variance, eddy viscosity, boundary layers

Layer Depths, Topography

In the interests of simplicity, layer depths in the text are sometimes rounded to the nearest 10 or 100 m. Thus for example, 2990 m is referred to as 3000 m. Table A.1 lists the model interface depths.

Approximate bathymetry as seen by the model is displayed in Fig. A1. Countless structures appear even with the comparatively coarse model resolution. Intricacy of real bottom topography can be computed from the gradient of h (not shown). A very large number of physical parameters enter when attempting to determine the time-mean response to flow over such irregularity. Complexity of the lateral boundaries, including shelves, re-entrant corners etc. will also persist into the flows at the longest possible time-scales. An underlying question, for which an answer is not readily forthcoming, is the extent to which the various imply that the model *should* be permitted to deviate from the interior data sets?
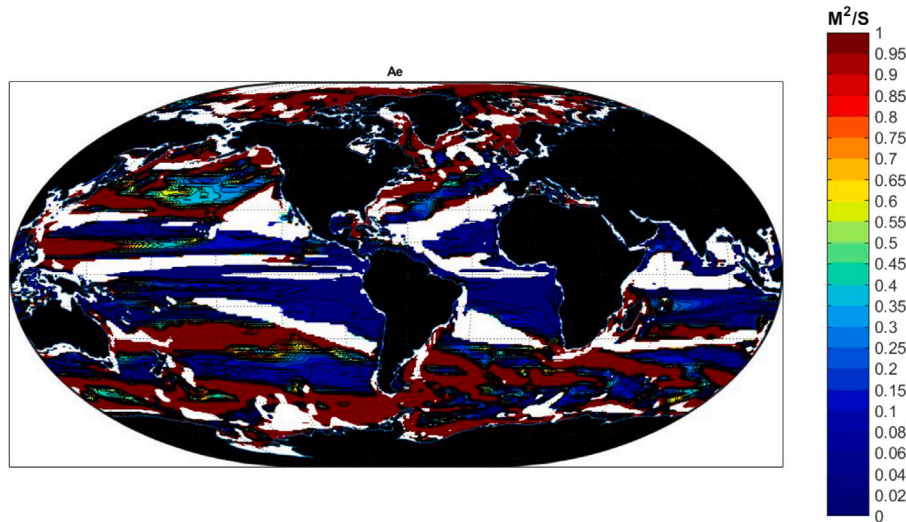
Fig. A4. Equivalent vertical eddy-viscosity coefficient A_v determined from the near-surface spiral. Units are m^2/s. In the blank areas, no estimate could be made that passed the ordinary significance test for the fit. Note that although some overlap exists with the structures in Fig. 15 they are not the same because the measures of fit differ. Colorbar saturates.
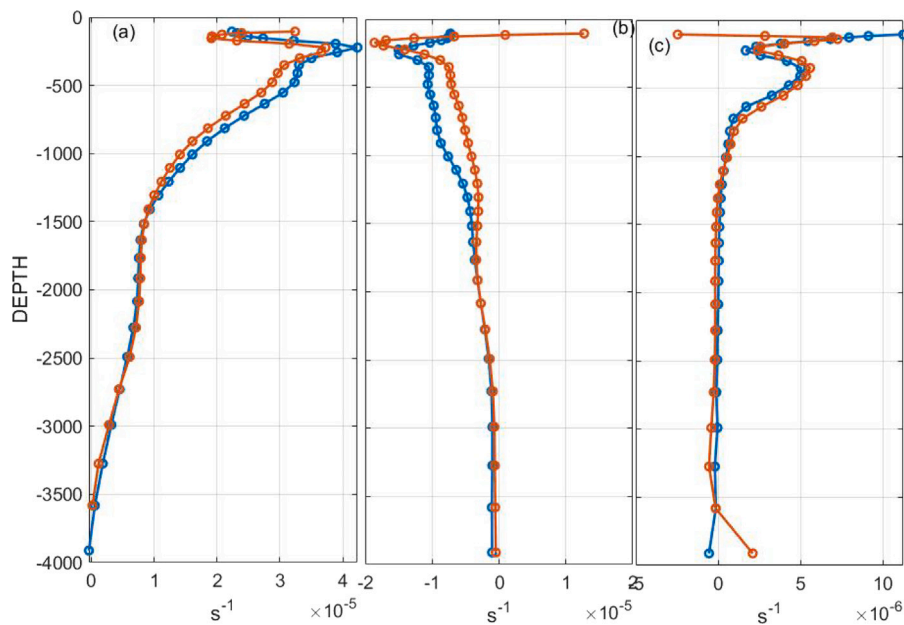

Fig. A5. Profiles below 100 m of the meridional thermal wind shear (blue) and the vertical derivative of v (red) at 60°S at three longitudes, 165°W, 121°W, 15°W showing that the major differences occur in the upper ocean.

Temporal Standard Deviation, Speed

The logarithm of the standard deviation of the surface speed about the 26-year mean as inferred from the underlying annual averages of u, v is shown in Fig. A2. High values appear generally where expected including the western boundary currents, the equatorial regions and the Southern Ocean. A similar calculation for temperature (not shown) displays markedly larger variability in the northern North Atlantic Ocean, and is presumably a consequence of sensitivity to variations in convective intensity, coupled with the long baroclinic adjustment times at high latitudes (e.g., Anderson and Gill, 1975).

Boundary Layers

Most of the available global-scale data concern the oceanic state lying outside the numerous boundary layers expected in the ocean at all surfaces including bottom topography, the sloping sidewalls, and the surface physics, and which are not resolved by the state estimate. The ECCO system, with the existing resolution, is an inverse problem

in which some parameters, e.g. temperature boundary values, are calculated from the observed interior solution. The Gulf Stream and other western boundary currents provide one example: these currents are not dynamically resolved in the state estimate. But if the interior flow is forced to consistency with resolved structures and it drives a boundary current mass or volume transport, e.g. through a Sverdrup-relation, then the interior property structures and transports of the system may well be accurately determined without complete dynamical consistency in the boundary layers. Much finer-scale boundary layers that are required to satisfy the no-flux and no-slip conditions at topography are implicitly parameterized without, it is assumed, doing violence to the data-constrained interior solution.

Rossby Number

Fig. A3 displays the logarithm of the estimated Rossby number at two depths. It tends to be very small at these and all other depths apart from the equatorial singularity.
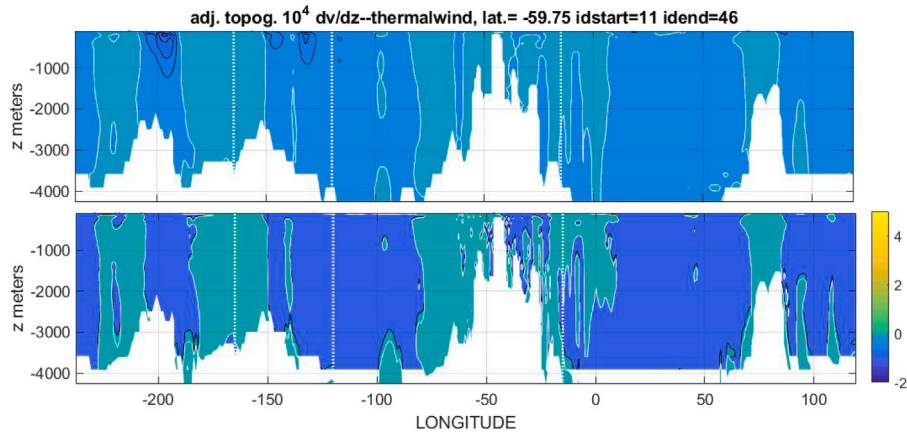
Fig. A6. 60°S thermal wind shear multiplied by f from the density field (upper panel) and dv/dz (lower panel). Difference between the two fields is greater here in the Southern Ocean than is seen at middle latitudes with a slight systematic difference in the southward going regions. Centered differences exaggerate the structural differences of apparent topography.
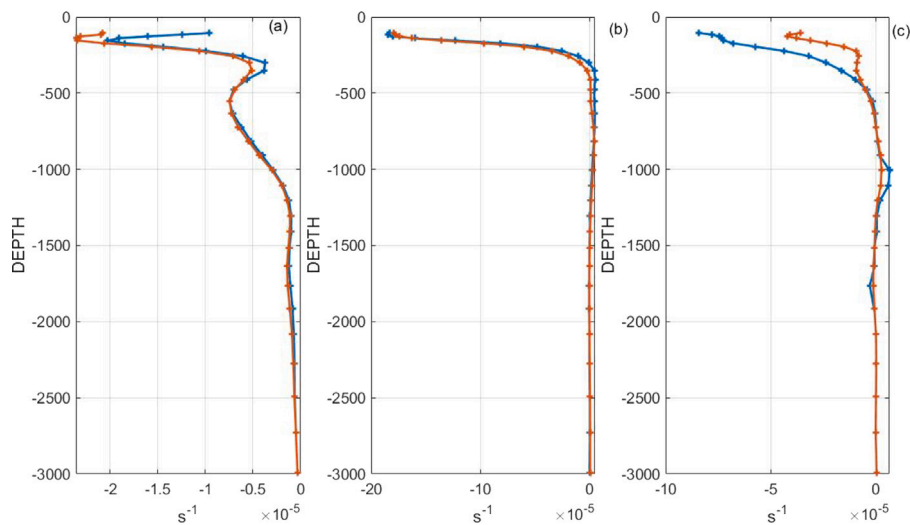

Fig. A7. Thermal wind profiles (blue) and du/dz (red) for velocity, v, profiles along 30°N in the three longitudes. Panels (a, b) are in the Pacific Ocean (at 169°W, 121°W) and (c) is a North Atlantic profile at 15°W. Shallowest depth is 100 m.
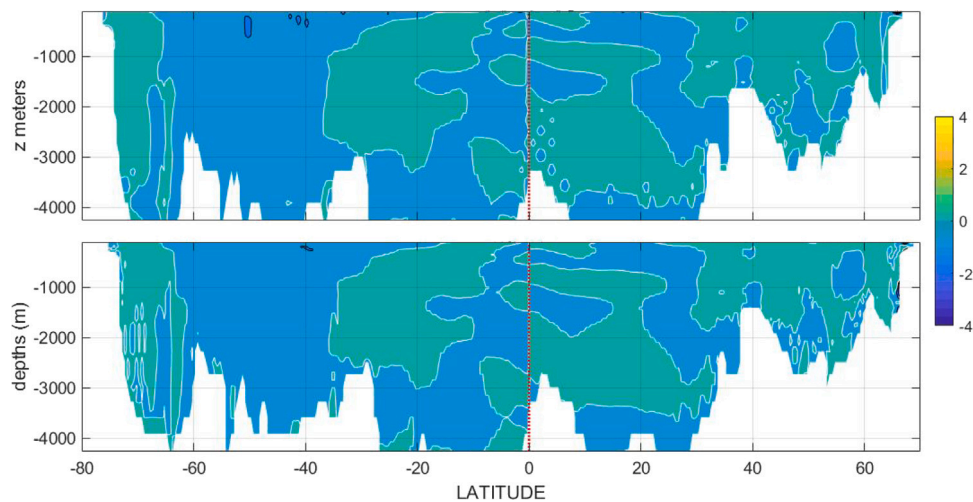

Fig. A8. Thermal wind shear (upper panel) and $f \partial u/\partial z$ (lower panel) along 30°W in the Atlantic, both multiplied by 10^8..

Equivalent vertical eddy-viscosity coefficients

The equivalent vertical eddy coefficient A_v corresponding to the Ekman spiral is shown in Fig. A4 and is markedly variable.

Thermal Wind Shear Profiles

Some of the deviations from perfect thermal wind balance in v at 60°S can be seen in Fig. A5. Fig. A6 shows the complete zonal structure (see Fig. A8).

References

Anderson, D.L.T., Gill, A.E., 1975. Spin-up of a stratified ocean, with applications to upwelling. Deep-Sea Res. 22, 583–596.

Berloff, P., Kamenkovich, I., Pedlosky, J., 2009. A mechanism of formation of multiple zonal jets in the oceans. J. Fluid Mech. 628, 395–425.

Brandt, P., Hormann, V., Bourles, B., Fischer, J., Schott, F.A., Stramma, L., Dengler, M., 2008. Oxygen tongues and zonal currents in the equatorial Atlantic. J. Geophys. Res.-Oceans 113.

Buzzicotti, M., Storer, B.A., Khatri, H., Griffies, S.M., Aluie, H., 2023. Spatio-temporal coarse-graining decomposition of the global ocean geostrophic kinetic energy. J. Adv. Mod. Earth Syst. 15.

Callies, J., Ferrari, R., 2018. Dynamics of an abyssal circulation driven by bottom-intensified mixing on slopes. J. Phys. Oceanogr. 48, 1257–1282.

Carroll, D., Menemenlis, D., Dutkiewicz, S., Lauderdale, J.M., Adkins, J.F., et al., 2022. Attribution of space–time variability in global-ocean dissolved inorganic carbon. Glob. Biogeochem. Cycl. 36, e2021GB007162.

Chen, R., Flierl, G.R., Wunsch, C., 2015. Quantifying and interpreting striations in a subtropical gyre: a spectral perspective. J. Phys. Oceanogr. 45, 387–406.

Cornillon, P., Firing, E., Thompson, A.F., Ivanov, L.M., Kamenkovich, I., Buckingham, C.E., Afanasyev, Y.D., 2019. In: Galperin, B.R., Read, P.L. (Eds.), Oceans. Zonal Jets. Phenomenology, Genesis and Physics. Camb. Un. Press, pp. 46–71.

Davis, R.E., 2005. Intermediate-depth circulation of the Indian and south Pacific oceans measured by autonomous floats. J. Phys. Oceanogr. 35, 683–707.

DeSanto, J.B., Sandwell, D.T., 2019. Meter-scale seafloor geodetic measurements obtained from repeated multibeam sidescan surveys. Mar. Geod. 42 (6), 491–506. http://dx.doi.org/10.1080/01490419.2019.1661887.

Ekman, V.W., 1905. On the influence of the Earth's rotation on ocean-currents. Ark. Mat., Astron. Fys. 2 (11), 52.

Forget, G., 2010. Mapping ocean observations in a dynamical framework: A 2004-06 ocean atlas. J. Phys. Oceanogr. 40, 1201–1221.

Forget, G., Campin, J.-M., Heimbach, P., Hill, C., Ponte, R., Wunsch, C., 2015. ECCO version 4: an integrated framework for non-linear inverse modeling and global ocean state estimation. Geosci. Model Dev. 8, 3071–3104.

Fukumori, I., Heimbach, P., Ponte, R.M., Wunsch, C., 2018. A dynamically-consistent ocean climatology and its temporal variations. Bull. Am. Meteorol. Soc. 2107–2127.

Fukumori, I., Wang, O., Fenty, I., Forget, G., Heimbach, P., Ponte, R.M., 2019. ECCO version 4 release 4. https://ecco.jpl.nasa.gov/drive/files\protect\discretionary{\char\hyphenchar\font}{}{}/Version4/Release4/doc/v4r4_synopsis.pdf.

Galperin, B., Read, P.L. (Eds.), 2019. Zonal Jets: Phenomenology, Genesis, and Physics. Cambridge Un. Press, Cambridge.

Garabato, A.C.N, Yu, X., Callies, J., Barkan, R., Polzin, K.L., Frajka-Williams, E.E., Buckingham, C.E., Griffies, S.M., 2022. Kinetic energy transfers between mesoscale and submesoscale motions in the open ocean's upper layers. J. Phys. Oceanogr. 52, 75–97.

Gaspar, P., Grègoris, Y., Lefevre, J.M., 1990. A simple eddy kinetic energy model for simulations of the oceanic vertical mixing: Tests at station papa and long-term upper ocean study site. J. Geophys. Res.-Oceans 95, 16179–16193.

Gebbie, G., 2021. Combining modern and paleoceanographic perspectives on ocean heat uptake. Ann. Revs. Mar. Sci. 13, 16.1–16.27.

Gent, P.R., Mcwilliams, J.C., 1990. Isopycnal mixing in ocean circulation models. J. Phys. Oceanogr. 20, 150–155.

Hogg, N.G., Owens, W.B., 1999. Direct measurement of the deep circulation within the Brazil basin. Deep-Sea Res. II 46, 335–353.

Huang, R.X., 2010. Ocean Circulation: Wind-Driven and Thermohaline Processes. Cambridge University Press., Cambridge, New York, p. xiii, 791.

Leetmaa, A., Niiler, P., Stommel, H., 1977. Does the sverdrup relation account for the mid-atlantic circulation? J. Mar. Res. 35, 1–10.

Liang, X., Spall, M., Wunsch, C., 2017. Global ocean vertical velocity from a dynamically consistent ocean state estimate. J. Geophys. Res.-Oceans 122, 8208–8224.

Losch, M., Heimbach, P., 2007. Adjoint sensitivity of an ocean general circulation model to bottom topography. J. Phys. Oceanogr. 37, 377–393.

Mazloff, M.R., Heimbach, P., Wunsch, C., 2010. An eddy-permitting southern ocean state estimate. J. Phys. Oceanogr. 40, 880–899.

McDougall, T.J., 1995. The influence of ocean mixing on the absolute velocity vector. J. Phys. Oceanogr. 25, 705–725.

McWilliams, J.C., Huckle, E., Liang, J.H., Sullivan, P.P., 2012. The wavy Ekman layer: Langmuir circulations, breaking waves, and Reynolds stress. J. Phys. Oceanogr. 42, 1793–1816.

Menemenlis, D., Campin, J.M., Heimbach, P., Hill, C., Lee, T., Nguyen, A., Schodlok, M., Zhang, H., 2008. ECCO2: High resolution global ocean and sea ice data synthesis. Mercat. Oceanogr. Q. Newsl. 31, 13–21.

de Miranda, A.P., Barnier, B., Dewar, W.K., 1999. On the dynamics of the Zapiola Anticyclone. J. Geophys. Res.-Oceans 104, 21137–21149.

Munk, W., Armi, L., Fischer, K., Zachariasen, F., 2000. Spirals on the sea. Proc. Roy. Soc. A 456, 1217–1280.

Nguyen, A.T., Pillar, H., Ocana, V., Bigdeli, A., Smith, T.A., Heimbach, P., 2021. The arctic subpolar gyre state estimate: Description and assessment of a data-constrained, dynamically consistent ocean-sea ice estimate for 2002–2017. J. Adv. Model. Earth Syst. 13, http://dx.doi.org/10.1029/2020MS002398.

Olbers, D., Willebrand, J., Eden, C., 2012. Ocean Dynamics. Springer, Berlin, New York, 1 e (xxiii, 704 p.).

Pedlosky, J., 1982. Geophysical Fluid Dynamics. Springer Verlag, xii, 624 pp.

Pedlosky, J., 1996. Ocean Circulation Theory. Springer, Berlin, New York, xi, 453 pp.

Phillips, N.A., 1963. Geostrophic motion. Rev. Geophys. 1, 123–176.

Price, J.F., Weller, R.A., Pinkel, R., 1986. Diurnal cycling: Observations and models of the upper ocean response to diurnal heating, cooling, and wind mixing. J. Geophys. Res.-Oceans 91, 8411–8427.

Price, J.F., Weller, R.A., Schudlich, R.R., 1987. Wind-driven ocean currents and Ekman transport. Science 238, 1534–1538.

Radko, T., 2023. A generalized theory of flow forcing by rough topography. J. Fluid Mech. 961. http://dx.doi.org/10.1017/jfm.2023.169.

Redi, M.H., 1982. Oceanic isopycnal mixing by coordinate rotation. J. Phys. Oceanogr. 12, 1154–1158.

Rogers, M., Ferrari, R., Nadeau, L.-P., 2023. Mid-depth recipes. J. Phys. Oceanogr. 53, https://doi-org.libproxy.mit.edu/10.1175/JPO-D-22-0225.1.

Roquet, F., Wunsch, C., 2022. The atlantic meridional overturning circulation and its hypothetical collapse. Tellus A 74, 393–398. http://dx.doi.org/10.16993/tellusa.679.

Roquet, F., Wunsch, C., Madec, G., 2011. On the patterns of wind-power input to the ocean circulation j. Phys. Oc. 41, 2328–2342.

Shrira, V.I., Almelah, R.B., 2020. Upper-ocean Ekman current dynamics: a new perspective. J. Fluid Mech. 887, A24–A27.

Stommel, H., Schott, F., 1977. The beta spiral and the determination of the absolute velocity field from hydrographic station data. Deep-Sea Res. 24, 325–329.

Talley, L.D., Pickard, G.L., Emery, W.J., 2011. Descriptive Physical Oceanography : An Introduction. Academic Press, Amsterdam, Boston, viii, 555 pp.

Tamsitt, V., Drake, H.F., Morrison, A.K., Talley, L.D., Dufour, C.O., Gray, A.R., Griffies, S.M., Mazloff, M.w R., Sarmiento, J.L., Wang, J., Weijer, W., 2017. Spiraling pathways of global deep waters to the surface of the Southern Ocean. Nature Comm. 8, 172.

Thomas, M.D., Boer, A.M. De, Johnson, H.L., Stevens, D.P., 2014. Spatial and temporal scales of sverdrup balance. J. Phys. Oceanogr. 44, 2644–2660.

Vallis, G.K., 2017. Atmospheric and Oceanic Fluid Dynamics: Fundamentals and Large-Scale Circulation, second ed. Cambridge Un. Press, 946 pp.

Wang, Q., Dong, C., Dong, J., Zhang, H., Yang, J., 2022. Submesoscale processes-induced vertical heat transport modulated by oceanic mesoscjale eddies. Deep-Sea Res. II 202, 105–138.

Wilson, E.A., Thompson, A.F., Stewart, A.L., Sun, S., 2022. Bathymetric control of subpolar gyres and the overturning circulation in the southern ocean. J. Phys. Oceanogr. 52, 205–223.

Wolfe, C.L., Cessi, P., 2010. What sets the strength of the middepth stratification and overturning circulation in eddying ocean models? J. Phys. Oceanogr. 40, 1520–1538.

Wunsch, C., 2023. A simplified ocean physics? Revisiting abyssal recipes. J. Phys. Oceanogr. 55, 1387–1400.

Wunsch, C., Ferrari, R., 2018. 100 Years of the ocean general circulation. Met. Monogr. 59, 7.1–7.32.

Wunsch, C., Heimbach, P., 2007. Practical global oceanic state estimation. Physica D 230, 197–208.

Wunsch, C., Williamson, S., Heimbach, P., 2023. Potential artifacts in conservation laws and invariants inferred from sequential state estimation. Ocean Sci. 19, 1253–1275.